

Article

Influence of the Thermal Treatment on the Structure and Cycle Life of Copper Hexacyanoferrate for Aqueous Zinc-Ion Batteries

Mohsen Baghodrat ¹, Giorgia Zampardi ^{1,*}, Jens Glenneberg ² and Fabio La Mantia ^{1,2,*}¹ Energiespeicher- und Energiewandlersysteme, Universität Bremen, Bibliothekstraße 1, 28359 Bremen, Germany² Fraunhofer Institute for Manufacturing Technology and Advanced Materials—IFAM, Wiener Straße 12, 28359 Bremen, Germany

* Correspondence: zampardi@uni-bremen.de (G.Z.); lamantia@uni-bremen.de (F.L.M.)

Abstract: Copper hexacyanoferrate (CuHCF) has become an attractive Zn^{2+} insertion material as a positive electrode in aqueous zinc-ion batteries thanks to its high reversibility towards Zn^{2+} (de-)insertion, its simple, inexpensive and easily scalable synthesis route, its low toxicity, and its high working potential. It is known that the physiochemical properties of CuHCF can be modified by manipulating its synthesis parameters. However, the effect of these parameters on the material's electrochemical performance and cycle life needs further investigation. Here, the structure and composition of CuHCF treated at different temperatures are studied through crystallographic, compositional, and thermogravimetric analyses. The resulting CuHCF powders were galvanostatically cycled to assess their electrochemical performance in relation to their annealing temperature. The results showed that the annealed CuHCF electrodes exhibited longer cycle life while maintaining a coulombic efficiency $\geq 99.5\%$. The longest cycle life was achieved by annealing the CuHCF electrodes at 100°C .

Keywords: aqueous zinc-ion batteries (ZIBs); copper hexacyanoferrate (CuHCF); cycle life; Prussian blue analogues (PBAs); thermal treatment



Citation: Baghodrat, M.; Zampardi, G.; Glenneberg, J.; La Mantia, F. Influence of the Thermal Treatment on the Structure and Cycle Life of Copper Hexacyanoferrate for Aqueous Zinc-Ion Batteries. *Batteries* **2023**, *9*, 170. <https://doi.org/10.3390/batteries9030170>

Academic Editor: Junnan Hao

Received: 1 February 2023

Revised: 1 March 2023

Accepted: 4 March 2023

Published: 15 March 2023



Copyright: © 2023 by the authors. Licensee MDPI, Basel, Switzerland. This article is an open access article distributed under the terms and conditions of the Creative Commons Attribution (CC BY) license (<https://creativecommons.org/licenses/by/4.0/>).

1. Introduction

To meet the increasing energy demands of current society, together with the need for independence from fossil fuels, it has become of critical importance to develop sustainable and low-cost methods to store electrical energy harvested from renewable sources [1–3]. Developing bulk energy-storage systems that meet the strict standards required by the stationary market in terms of high-rate capability, high safety, and low environmental impact is therefore essential for the cost-effective and sustainable integration of renewable energy into the power grid [4–8]. Aqueous metal-ion batteries are ideal candidates for such applications, as they are intrinsically cheap and safe energy-storage devices. However, they require further advancements to reach higher efficiency and longer cycle life, in order to compete with the more mature organic-based Li-ion technology [9–12].

In the current research on aqueous metal-ion batteries, there is a rising interest in developing aqueous Zn-ion batteries (A-ZIBs). The high specific power and high reversibility in aqueous solutions of these batteries, combined with their low cost, environmental friendliness, and earth-abundance of metallic zinc, have made them appealing choices for large-scale grid-energy-storage applications [5,6,13–17].

Despite the promising advantages of A-ZIBs, their commercial application remains limited due to the low efficiency of the zinc electrodeposition reaction occurring at the negative electrode [16,18] and the lack of suitable Zn-insertion materials for the positive electrode. To resolve the latter problem, it is crucial to consider different aspects, such as economics, safety, and ecology. Ideally, the cathode material needs to be non-toxic and

cost-effective, and, at the same time, highly durable when cycled in aqueous electrolytes without compromising its reversibility [4,9,19,20].

Among the insertion materials for the positive electrode of an A-ZIB, the hexacyanometallates of transition metals, generally known as Prussian blue analogues (PBAs), have generated significant interest due to their high reversibility towards the (de-)insertion of many cations, low volume changes during the ion-insertion reaction, low toxicity, and low costs [4,21–24]. As shown in Figure 1, the compounds belonging to the PBA family are characterized by an open-framework structure, with large cavities and channels created by two transition metals that are octahedrally linked together by CN ligands [25–27]. The face-centered cubic crystal lattices of PBAs allows the rapid movement of ions, enabling high-rate performance due to the fast (de-)insertion of a wide variety of ions, such as Li^+ , Na^+ , K^+ , Zn^{2+} , Mg^{2+} , and Al^{3+} [4,20,28–33].

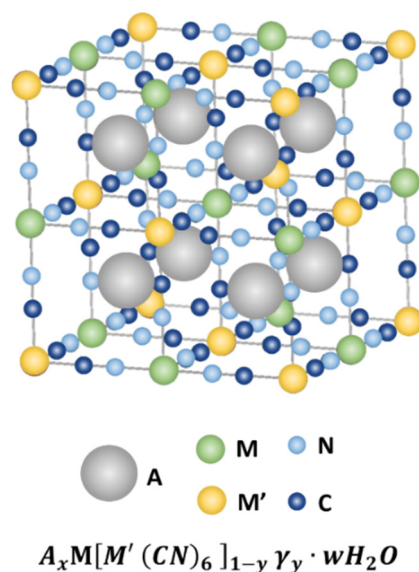


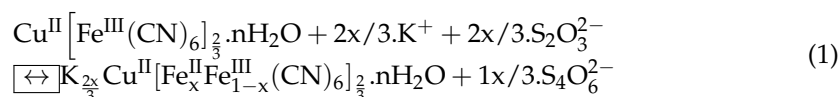
Figure 1. Schematic representation of the open-framework structure of a general PBA, where: A: alkaline cation, M, M': transition metals, C: carbon, N: nitrogen. The structural water molecules have been omitted for the sake of clarity.

Among the materials belonging to the PBA family, copper hexacyanoferrate (CuHCF) has attracted significant attention as an active material for the positive electrode in aqueous Zn-ion batteries since the first time it was used for this purpose, in 2015 [31].

Copper hexacyanoferrate shows high reversibility towards the (de-)insertion reaction of various monovalent, divalent, and trivalent ions in aqueous electrolytes [6,19,34]. It can be synthesized using abundant and non-toxic elements through a simple and inexpensive synthesis route that can be easily scaled up to an industrial level. Moreover, this material is well suited to power-grid applications because of its excellent power-rate capability and high cell-working potential, of about 1.7 V, compared with Zn^{2+}/Zn . The latter enables CuHCF-based A-ZIBs to utilize the electrochemical-stability window of water almost fully [30,34–37].

Despite its many advantages, CuHCF suffers from a relatively short cycle life when operated in rechargeable aqueous-based systems, compared to the commercial insertion materials employed in organic lithium-ion batteries. Interestingly, it has been observed that the stability and the electrochemical properties of CuHCF can be tuned by changing various parameters, such as the reaction time, the temperature, and the reactant concentration during the material-synthesis procedure. According to previous studies, these strategies mainly affect the positioning of the elements, the potassium or iron content, and the amount of coordinated (interstitial) water in the CuHCF lattice [6,20,35,38,39].

As part of our previous efforts to optimize CuHCF's properties [6], we adjusted the reactants' (i.e., $\text{Cu}(\text{NO}_3)_2$ and $\text{K}_3\text{Fe}(\text{CN})_6$) ratio and concentration during the synthesis of CuHCF. Our physicochemical analyses of our pristine CuHCF samples synthesized with different reactant concentrations and ratios indicated different potassium contents in the lattice. In particular, an increasing amount of potassium within the initial CuHCF lattice led to smaller bond distances, namely smaller crystal dimensions, resulting in the higher long-term stability of the material and, therefore, an improved cycle life. The initial potassium content within the lattice of CuHCF was also considered by Ojwang et al. [35,38,40]. In their work, $\text{K}_2\text{S}_2\text{O}_3$ was incorporated into the synthesis according to Equation (1).



Infra-red (IR) spectroscopy measurements associated with synchrotron-based experiments showed that a lower $\text{Fe}^{\text{III}}/\text{Fe}^{\text{II}}$ ratio in the lattice and smaller cell dimensions were associated with a higher initial potassium content. Variations in the $\text{Fe}^{\text{III}}/\text{Fe}^{\text{II}}$ ratio in the lattices of hexacyanometallates were also observed by Gerber et al. [41] while employing different precursors, such as Fe, Co, Ni, and Cu, in the coprecipitation reaction of their hexacyanoferrates. Their IR measurements revealed that the utilized metal precursor strongly influenced the peak position and the intensity of the $\text{Fe}^{\text{III}}\text{-CN}$ and of the $\text{Fe}^{\text{II}}\text{-CN}$ bands in the IR spectrum. In another study on the magnetic properties of CuHCF, by Ng et al. [42], variations in the $\text{Fe}^{\text{III}}/\text{Fe}^{\text{II}}$ ratio in the lattice were also observed while investigating the effects of thermal treatment on CuHCF's crystal structure. According to their findings, annealing the CuHCF powder led to the conversion of the material's microstructure from an initial composition of $\text{Fe}^{\text{III}}\text{-CN-Cu}^{\text{II}}$ to $\text{Fe}^{\text{II}}\text{-CN-Cu}^{\text{III}}$ and $\text{Cu}^{\text{II}}\text{-CN-Fe}^{\text{III}}$, with a progressive decrease in the lattice parameter.

In light of the studies mentioned above, both the crystal structure and the chemical composition of CuHCF can be modified by adjusting the synthesis parameters. Moreover, it appears that the potassium and the iron (either Fe^{II} or Fe^{III}) contents in the CuHCF lattice play a pivotal role in determining its unit cell's parameters. There are, however, only a few studies on how these modifications influence the electrochemical performance of the material. The tuning of the crystal structure of PBAs in general, and of CuHCF in particular, is primarily studied in non-battery research areas, and, therefore, assessments of the electrochemical performance are not routinely provided.

In our previous study, the highest initial potassium content related to the smallest unit cells was associated with the longest cycling lifetime of our CuHCF-based electrodes [6]. In this work, we addressed the question of how thermally induced structural changes influence the electrochemical performance of CuHCF. Here, CuHCF powder was synthesized via the routinely used coprecipitation method and thermally treated at various temperatures before its electrochemical testing in three-electrode flooded cells. Structural and chemical analyses were performed on the thermally treated CuHCF powders to correlate the effect of the annealing temperature with the changes in the material's crystal structure. Moreover, galvanostatic cycling of the CuHCF-based electrodes was performed to assess the material's cycle life as a function of its thermal treatment.

2. Experimental Methods

2.1. Material Synthesis

Copper hexacyanoferrate (CuHCF) was synthesized through the standard coprecipitation method reported in [43]. Briefly, under vigorous stirring at room temperature, two solutions, of 50 mM $\text{Cu}(\text{NO}_3)_2 \cdot 3\text{H}_2\text{O}$ (Sigma Aldrich, Munich, Germany) and 100 mM $\text{K}_3\text{Fe}(\text{CN})_6$ (Sigma Aldrich), were added simultaneously and dropwise to 60 mL of deionized water. A brown suspension was formed immediately, which was subsequently bath-sonicated for 30 min and then allowed to settle overnight. The formed precipitate was centrifuged and subsequently washed with a solution containing 1 M KNO_3 (Sigma

Aldrich) and 10 mM HNO₃ (Sigma Aldrich), followed by rinsing with deionized water, in order to eliminate any remaining impurities or unreacted precursors from the synthesis of the CuHCF. Subsequently, the drying of the CuHCF powder at 60 °C was carried out overnight. The resulting material was then ground using mortar and pestle.

2.2. Electrochemical Characterization

The electrochemical measurements were carried out using a BioLogic VMP3 instrument in a flooded three-electrode cell consisting of a CuHCF-based working electrode, two zinc foils (99.99%, Good Fellow) as counter and reference electrodes, and a 100-millimolar ZnSO₄ (Heptahydrate, 99.95%, Sigma Aldrich) aqueous solution as electrolyte. The working electrodes were prepared by hand brushing the CuHCF-based slurry on carbon cloth (Fuel Cell Earth) current collector with a mass loading of approximately 10 mg cm^{−2}. To make the slurry, CuHCF powder, amorphous carbon (Super C65, Timcal), polyvinylidene fluoride (PVdF) (Solef S5130, Solvay, Brussels, Belgium), and graphite (SFG6, Timcal) were dispersed in N-methyl-2-pyrrolidone (NMP) (Sigma Aldrich) with a weight ratio of 80:9:9:2. The dispersion was then mixed thoroughly for 30 min at 4000 rpm using an Ultra-Turrax disperser (T10, IKA). Prior to the assembly of the electrochemical cells, the CuHCF-based working electrodes were annealed at 60°, 80°, 100°, 120°, and 150 °C for 6 h under vacuum. Before each electrochemical test, the open-circuit potential was measured for one minute.

2.3. Material Characterization

The thermo-gravimetric properties of the CuHCF were studied using a NETZSCH STA 449 F3 thermogravimetric analyzer under an inert argon atmosphere at 35–250 °C (5 K min^{−1} rate) in Al₂O₃ crucibles.

Prior to the scanning electron microscopy (SEM), IR spectroscopy analysis and X-ray powder diffraction (XRPD), pristine CuHCF powder samples were annealed under the same thermal conditions as the electrodes (namely, at 60°, 80°, 100°, 120°, and 150 °C for 6 h under vacuum). The attenuated total reflectance infrared Fourier transform (ATR-FTIR) spectra were generated and acquired using a Bruker ALPHA II compact spectrometer configured in the mid-IR range. The spectra were acquired with a resolution of 2 cm^{−1}.

To record the XRPD patterns, a Miniflex Rigaku[®] diffractometer was utilized, with CuKα radiation at room temperature in the 2θ range of 10–60° at a scan speed of 5 s per step and a step width of 0.03°. A quartz holder was used without the help of any solvents to hold the powder sample. The diffractograms were normalized based on their highest peak intensity.

The SEM images were acquired using a FEI Helios NanoLan 600 DualBeam[®] apparatus with an acceleration voltage of 10 kV. To overcome the inadequate electronic conductivity of the particles, platinum/palladium coatings were employed.

3. Results and Discussion

Initially, the thermal stability of our synthesized CuHCF powder was analyzed with a thermogravimetric analyzer between 35 °C and 250 °C. The thermogravimetric analysis (TGA) was carried out under an inert argon atmosphere. As observed in the thermogravimetric curve reported in Figure 2, upon increasing the temperature, the CuHCF powder showed a mass loss, which slowly started at around 80 °C and was continuous until a temperature of ca. 170 °C was reached. When the CuHCF powder was exposed to a temperature of 148 °C, a sharp, exothermic peak appeared in the corresponding differential scanning calorimetry (DSC) curve. This exothermic peak was attributed to the rapid decomposition of the cyanide groups present in the CuHCF lattice [42,44], which led to the significant degradation of its crystal structure. It is worth noticing that an initial partial decomposition of cyanide groups might start even at temperatures lower than 148 °C. However, the initial decomposition starting point may vary between CuHCF samples synthesized through different synthesis routes and reactant concentrations [42,44]. Based on the peak location on the DSC curve, it appears that our pristine CuHCF powder was

stable up to nearly 120 °C, after which it slowly started to partially degrade until completely losing its stability at temperatures ≥ 150 °C.

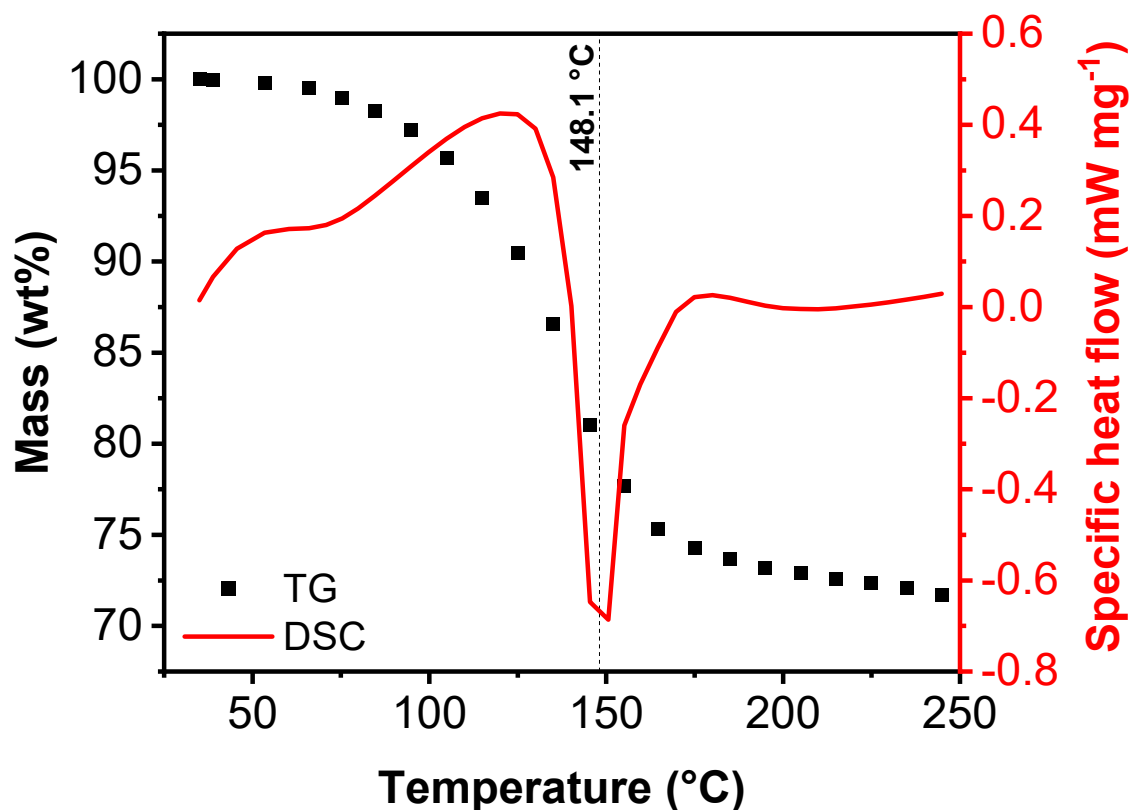


Figure 2. Thermogravimetric curve (black) and differential-scanning-calorimetry curve (red) of the synthesized CuHCF powder.

Successively, the synthesized CuHCF powders were annealed at different temperatures, namely 60°, 80°, 100°, 120°, and 150 °C. A structural analysis was performed on all the thermally treated CuHCF powders and the untreated powder. The X-ray powder diffractograms of all the analyzed powders (Figure 3) showed a pattern corresponding to an F-centered cubic unit cell (fm3m space group), which was in agreement with the primary reflections corresponding to $K_{2x/3}Cu[Fe(CN)_6]_{2/3} \cdot nH_2O$ [38].

Despite the similarities in the XRPD patterns of all the analyzed CuHCF powders, a slight 2θ shift and a change in the peak intensity ratio of the 220/200 planes (I_{220}/I_{200}) were observed when increasing the annealing temperature. The shift of the 220 and 200 reflections towards higher 2θ values appeared more prominent when the CuHCF powder was annealed at 120 °C and 150 °C compared to the other thermally treated samples. The changes in the crystal parameters are shown more clearly in Figure 4, which represents the variations in the I_{220}/I_{200} peak-intensity ratio and the lattice constant in the dependency on the temperature employed during the annealing of the CuHCF powders. These results are in agreement with those of previous works [6,38,42,45]; accordingly, the increased I_{220}/I_{200} ratio and the shift of the peaks to higher 2θ values indicate a rearrangement of the elements in the structure towards a smaller crystal unit [6,35,38,40].

The SEM analysis showed that there were no significant variations in the average particle sizes or the morphologies of all the thermally treated CuHCF powders (Figure S1), which resembled those of the untreated CuHCF shown in Figure 5.

The ATR-FTIR spectra of all the investigated CuHCF samples are shown in Figure 6. The cyanide complex can be easily identified as sharp bands stretching between 2000 cm^{-1} and 2200 cm^{-1} [38]. Interestingly, with the Prussian blue analogues, it is possible to differentiate between the ferrocyanide ($Fe^{II}\text{-CN}$) and ferricyanide ($Fe^{III}\text{-CN}$) groups in the

IR spectrum because of the C-N band position. Due to the higher oxidation number of the Fe and the stronger σ -bond, the positions of $\text{Fe}^{\text{III}}\text{-CN}$ bond peaks are expected to appear at higher wavenumbers than the peaks of $\text{Fe}^{\text{II}}\text{-CN}$ bonds [38]. The two peaks at 2100 cm^{-1} and 2170 cm^{-1} in Figure 6 indeed correspond to the $\text{Fe}^{\text{II}}\text{-CN-Cu}^{\text{II}}$ and the $\text{Fe}^{\text{III}}\text{-CN-Cu}^{\text{II}}$ groups of the CuHCF lattice, respectively. Upon increasing the temperature employed during the thermal treatment of the material, a significant change in the relative peak intensities of the $\text{Fe}^{\text{III}}\text{-CN}$ and the $\text{Fe}^{\text{II}}\text{-CN}$ peaks was clearly observed. In particular, as the temperature increased, the intensity of the 2170 cm^{-1} band ($\text{Fe}^{\text{III}}\text{-CN-Cu}^{\text{II}}$) diminished, while the intensity of the 2100 cm^{-1} band ($\text{Fe}^{\text{II}}\text{-CN-Cu}^{\text{II}}$) increased. When a temperature of $150\text{ }^{\circ}\text{C}$ was chosen for the annealing, the $\text{Fe}^{\text{III}}\text{-CN-Cu}^{\text{II}}$ band almost disappeared and, at the same time, the $\text{Fe}^{\text{II}}\text{-CN-Cu}^{\text{II}}$ band displayed a broad shoulder extending to wavenumbers as low as 2020 cm^{-1} . According to other studies [38,42], this shoulder can be attributed to $\text{Cu}^{\text{II}}\text{-CN-Fe}^{\text{II}}$, and it is expected to be observed at slightly lower wavenumbers than $\text{Fe}^{\text{II}}\text{-CN-Cu}^{\text{II}}$ due to the higher electronegativity of Cu^{II} compared to Fe^{II} and the lower σ -donation.

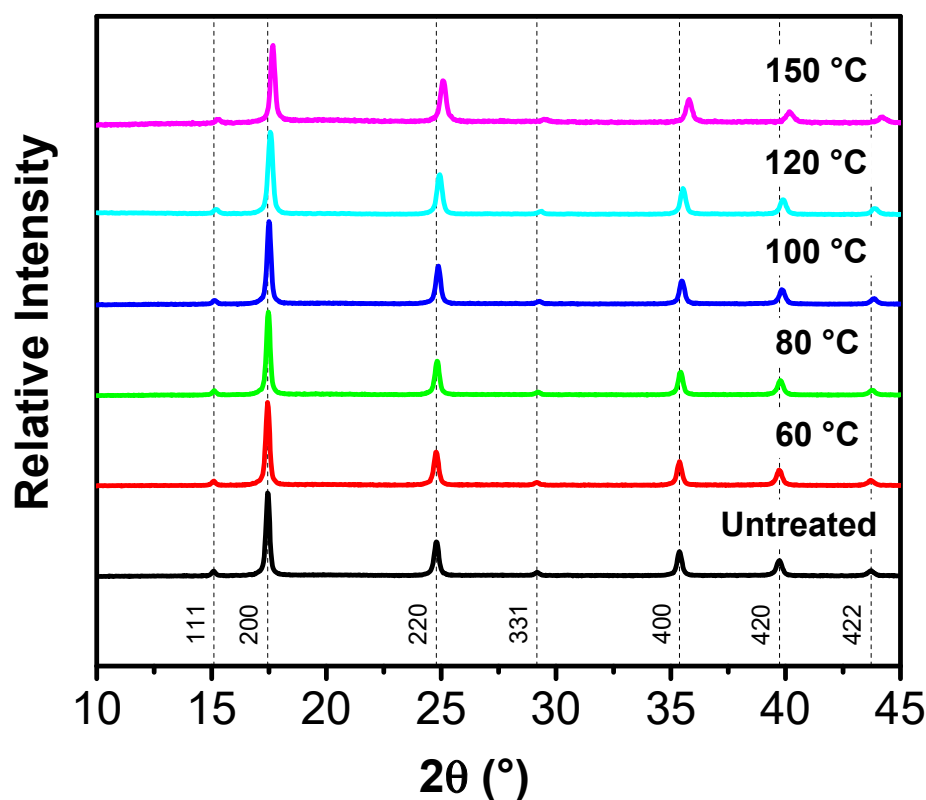


Figure 3. The XRPD patterns of the CuHCF powders thermally treated at different temperatures.

From the analysis of the ATR-FTIR spectra, it is possible to extract the relative amount of Fe^{III} with respect to the total iron content of the lattice based on the ratio between the 2100 cm^{-1} and the 2170 cm^{-1} bands' intensities. As shown in Figure 7, in the case of the untreated CuHCF powder, the oxidation state of the Fe was primarily (+3). By contrast, when the CuHCF powders were treated with increasing temperatures, the relative amount of Fe^{III} decreased, and the amount of Fe^{II} increased. This trend followed a similar pattern as the lattice constant (Figure 4a), in which increasing the treatment temperature caused the unit cell to shrink. Therefore, it appears that the thermal treatment might have caused a rearrangement of the CuHCF crystal structure, which may have led to a change in the amount and/or type of defects present in the lattice, ultimately resulting in the reduction of a portion of the Fe^{III} present in the crystal structure. However, further investigations are needed to clarify the role of annealing in this change in the oxidation state of the iron atoms in CuHCF lattices.

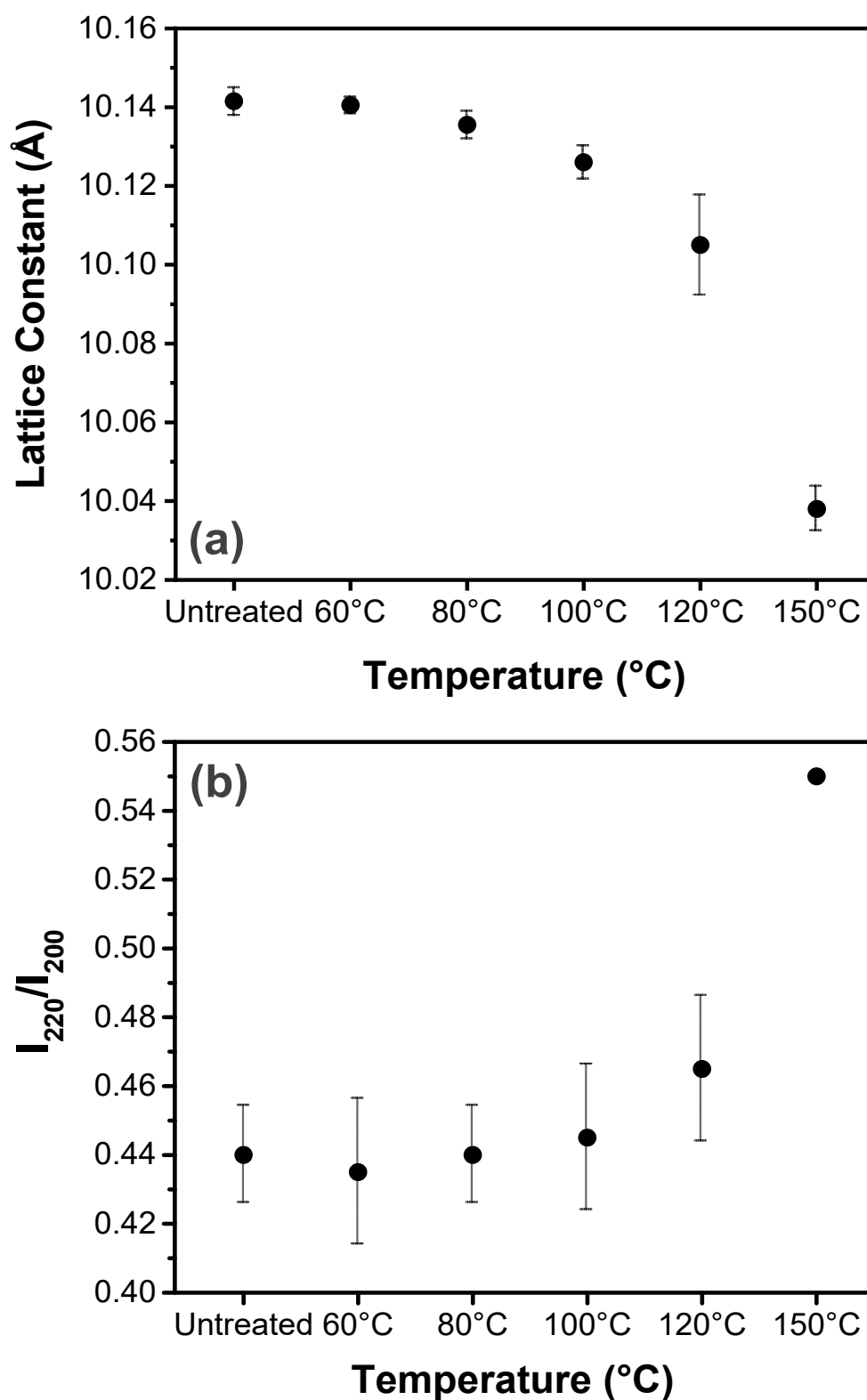


Figure 4. (a) Average lattice constant of the CuHCF powder as a function of the temperature employed during the thermal treatment, (b) average variation in X-ray-diffraction-intensity ratio between 220 and 200 planes (I_{220}/I_{200}) of the CuHCF powder as a function of the temperature employed during the thermal treatment. The mean values and standard deviations were estimated by comparing at least two different samples resulting from two different thermally treated CuHCF powders.

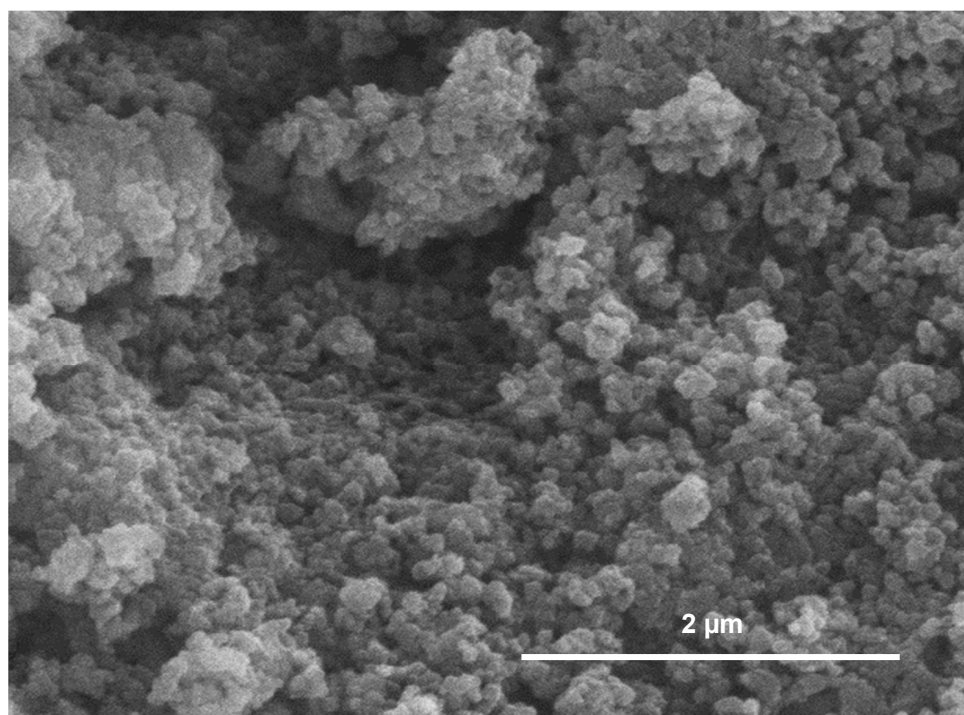


Figure 5. SEM image of untreated CuHCF powder.

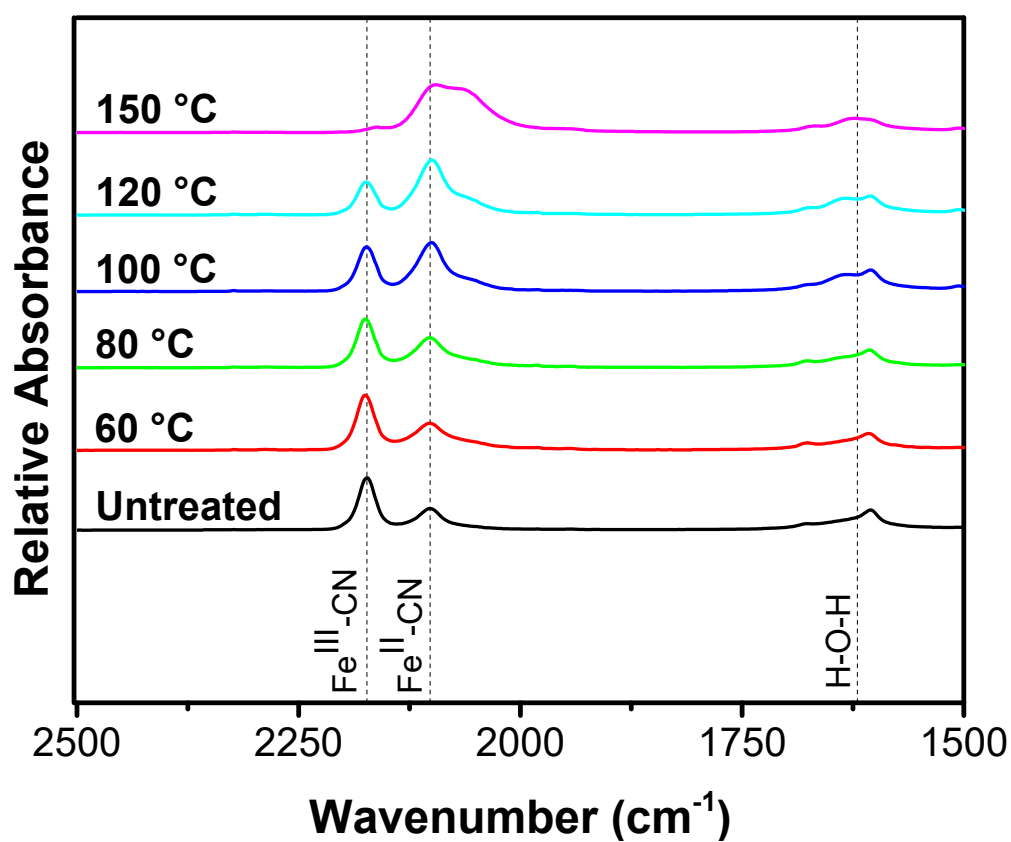


Figure 6. The ATR-FTIR spectra of the synthesized CuHCF powders thermally treated at different temperatures.

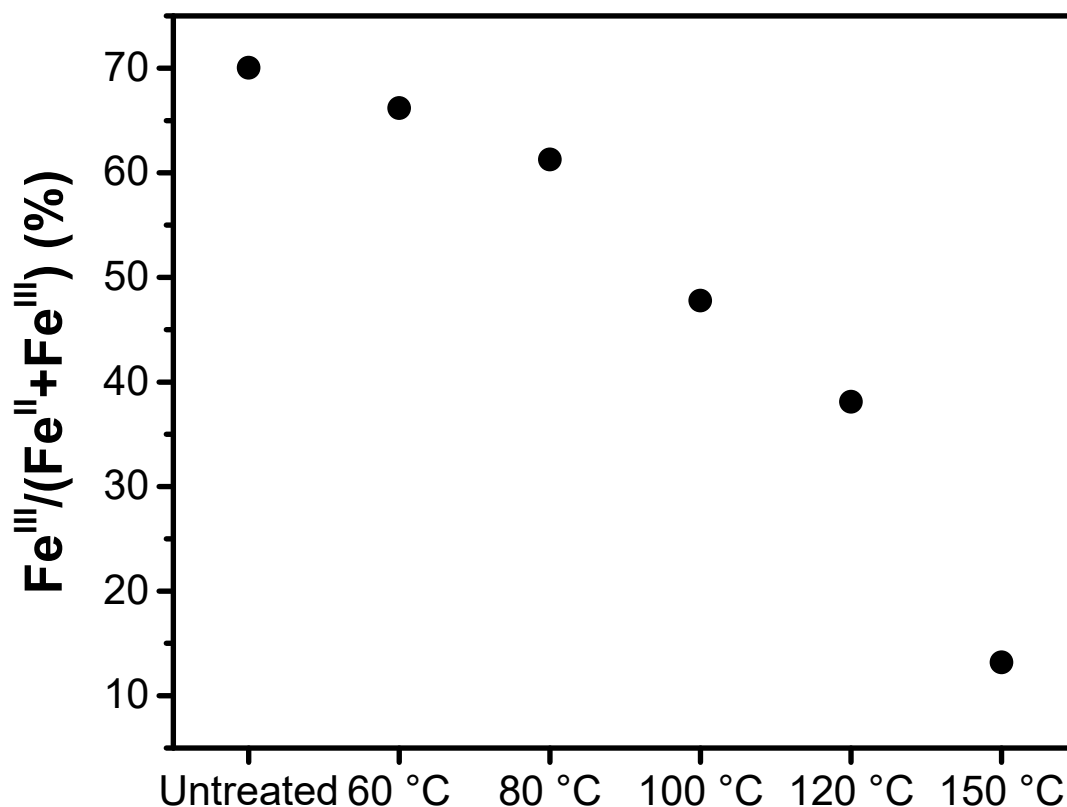


Figure 7. Fraction of Fe^{III} with respect to the total iron content of the lattice as a function of the temperature employed during the treatment of the CuHCF powder.

It is worth noting that within the FTIR spectra, a broad peak was observed for all the investigated samples at around 1600 cm^{-1} , which was attributed to the interstitial water content within the material's lattice [44,46]. In agreement with the literature [39,42], the FTIR spectra demonstrated that the annealing of the CuHCF up to 140 °C had little effect on the amount of interstitial water, but it primarily eliminated the water adsorbed on the material surface. The intensity of the peak at 1600 cm^{-1} displayed negligible fluctuations with increasing temperatures up to 100 °C , particularly in comparison with the variations observed in the intensity of the peaks at 2100 and 2170 cm^{-1} . This suggests that the thermal treatment had a more significant effect on the relative Fe^{III}-to-Fe^{II} content than on the interstitial water.

The electrochemical performance of the annealed CuHCF electrodes was assessed through galvanostatic cycling in the 100 mM ZnSO_4 aqueous solutions at a current rate (C-rate) of 1C. This C-rate was chosen considering that the usual operational currents required by a storage device for the power grid range from 0.5C to 2C [5,47]. According to Table 1, the initial specific discharge capacity ($Q_{0,\text{discharge}}$) decreased slightly when increasing the annealing temperature. In particular, the CuHCF electrode annealed at 150 °C showed an extremely low initial discharge capacity, of 15.2 mAh g^{-1} . This was a direct consequence of the irreversible degradation of the material's crystal structure at this temperature, as previously shown through the thermogravimetric analysis (Figure 2).

Interestingly, the open-circuit potential (OCP) of the annealed CuHCF electrodes decreased when increasing the annealing temperature. Indeed, before cycling, as the annealing temperature increased, the amount of Fe^{II} became predominant within the lattice, while the amount of Fe^{III} decreased. Consequently, the OCP value shifted towards lower potentials due to the lower electronegativity of the Fe^{II}.

Table 1. Open-circuit potential, average amount of charge exchanged at full state of charge in the first cycle, average initial discharge capacity, average initial discharge energy, and average cycle life based on discharge capacity and discharge energy of all the synthesized CuHCF-based electrodes. The errors in OCP measurements are within ± 5 mV. All the values reported within this table were averaged by comparing at least two different samples resulting from two different thermally treated CuHCF powders.

Treatment Temperature ($^{\circ}\text{C}$)	OCP (V)	$Q_{0,\text{charge}}$ (mAh g^{-1})	$Q_{0,\text{discharge}}$ (mAh g^{-1})	$E_{0,\text{discharge}}$ (mWh g^{-1})	Cycle Life Based on $Q_{\text{discharge}}$	Cycle Life Based on $E_{\text{discharge}}$
Untreated	1.69	13.6 ± 1.3	58.1 ± 1.3	92.5 ± 2.1	170	190
60	1.67	19.6 ± 0.2	56.4 ± 0.2	89.6 ± 0.2	210	320
80	1.65	21.8 ± 0.2	54.6 ± 0.2	87.0 ± 0.4	280	350
100	1.62	29.4 ± 0.2	54.5 ± 0.2	87.4 ± 0.4	340	400
120	1.48	46.6 ± 1.9	49.8 ± 1.9	83.3 ± 0.8	290	340
150	1.32	-	15.2 ± 1.2	26.3 ± 2.1	-	-

Figure S2 shows further proof of the increase in the Fe^{II} content in the CuHCF lattice upon increasing the annealing temperature. Indeed, the initial oxidation charge in the annealed CuHCF electrodes that was needed to reach the fully charged state during the first cycle ($Q_{0,\text{charge}}$) increased upon increasing the annealing temperatures, due to the higher initial amount of Fe^{II} that could be oxidized to Fe^{III} . Both the decrease in the OCP and the increase in the initial $Q_{0,\text{charge}}$ represent electrochemical proofs ascribed to the increase in the initial Fe^{II} content in the CuHCF lattice, which is in agreement with the ATR-FTIR analysis (Figure 7).

The long-term galvanostatic cycling of the CuHCF electrodes also changed depending on the annealing temperature (Figure 8). In particular, the cycle life of the CuHCF increased with the increase in the annealing temperature up to 100°C . However, it gradually decreased when annealed at temperatures higher than 100°C . As shown in Figure 8a, the 100°C sample retained 80% of its initial discharge capacity after 340 cycles, whereas the untreated electrode achieved the same capacity retention only after 170 cycles.

The CuHCF electrode annealed at 120°C exhibited a shorter lifespan, of around 290 cycles. Interestingly, the standard deviation in the capacity retention along the cycles was more significant for the 120°C sample than that the other annealed electrodes. This evident variation in the electrochemical behavior of the CuHCF annealed at 120°C can be explained by taking into consideration the TG curve (Figure 2): at this temperature, it appears that an initial partial degradation of the CuHCF lattice started to occur, and this may have caused a lower stability in the CuHCF crystal structure when cycled electrochemically. Thus, we believe that both the shorter lifespan and the larger standard deviation were probably due to the start of this partial degradation of the material lattice at 120°C .

The initial specific discharge energy ($E_{0,\text{discharge}}$) of all the CuHCF electrodes ranged around $80\text{--}90 \text{ mWh g}^{-1}$ (Table 1), except the electrode annealed at 150°C . In the case of the initial discharge capacity, the initial specific energy also slightly decreased with the increasing annealing temperature. In the case of the electrode annealed at 150°C , the low initial specific energy was due to the degradation of the material lattice that occurred at this temperature, as discussed above.

As with the discharge-capacity retention, the specific energy retention was strongly influenced by the annealing temperature of the CuHCF-based electrodes (Figure 8b). Similarly, the CuHCF electrode annealed at 100°C reached 80% energy retention after 400 cycles, compared to the 190 cycles retained by the untreated CuHCF.

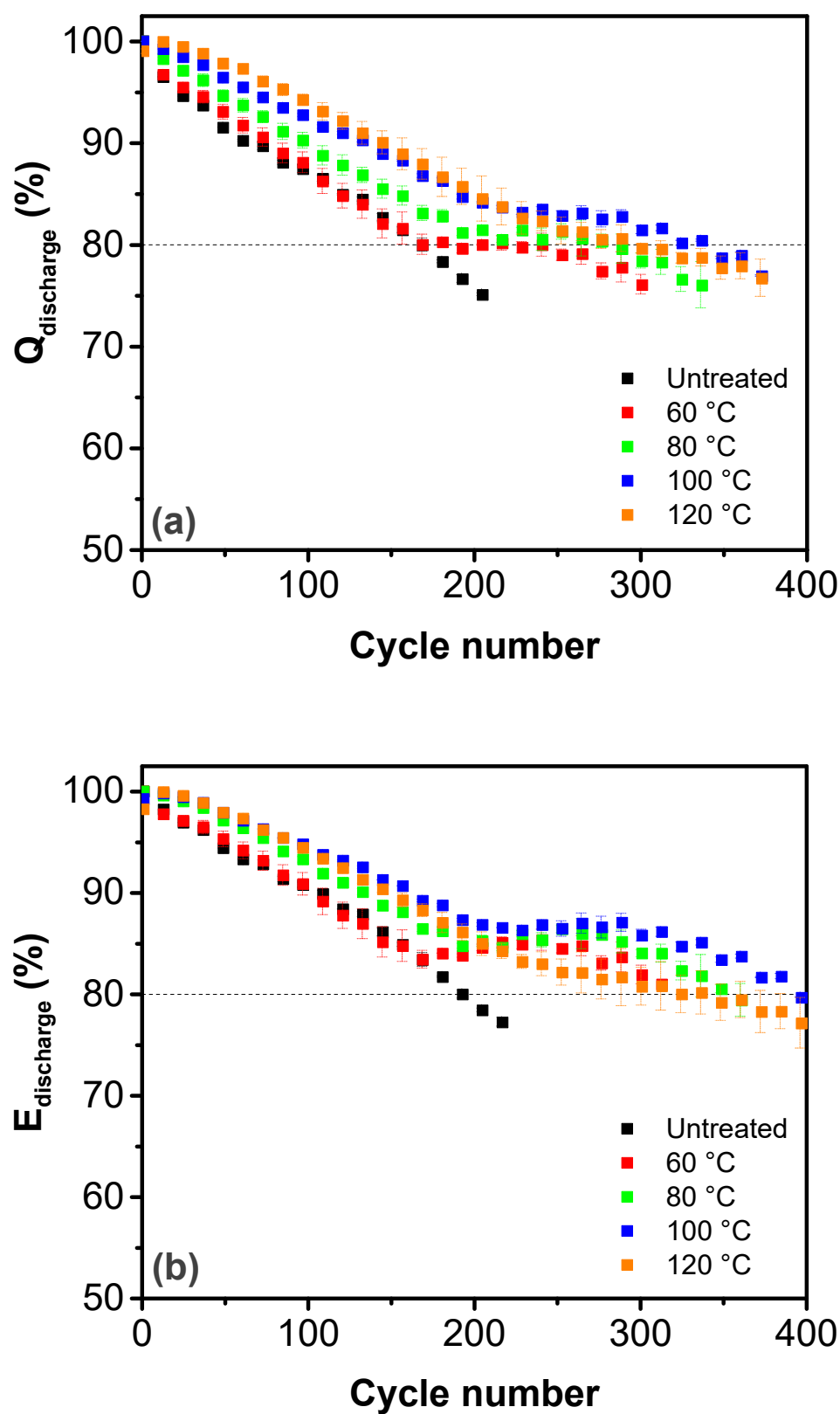


Figure 8. Mean value and standard deviation of (a) specific discharge-capacity retention and (b) specific discharge-energy retention of the synthesized CuHCF-based electrodes galvanostatically cycled at 1C annealed at different temperatures. The mean value and the standard deviations were calculated according to at least two different measurements of two different synthesis batches for each annealing temperature.

It is generally known that the cycle life of CuHCF in terms of delivered energy density is longer than that estimated in terms of the electrode's specific capacity. This behavior can be explained by examining the potential profiles derived from galvanostatic measurements. Figure 9 and Figure S3 illustrate the potential profiles of a selection of cycles for both the untreated CuHCF-based electrode and the annealed electrodes. In all cases, a plateau appeared at 1.6 V vs. Zn^{2+}/Zn at the beginning of the charge curve, which was due to the $\text{Fe}^{\text{III}}/\text{Fe}^{\text{II}}$ redox associated with the (de-)insertion of the Zn^{2+} . However, the (de-)insertion potential was partially shifted towards higher values, at approximately 1.7 V vs. Zn^{2+}/Zn , with the material cycling. This higher insertion plateau enabled a two-phase Zn^{2+} insertion in the CuHCF lattice. This can be more clearly visualized with the aid of the differential charge plots (Figure 10 and Figure S4). Here, two pairs of peaks can be observed at 1.6 V vs. Zn^{2+}/Zn and 1.7 V vs. Zn^{2+}/Zn . Notably, the first pair of peaks, at 1.6 V vs. Zn^{2+}/Zn , was present from the beginning of the cycling of both electrodes, whereas the second pair of peaks, at 1.7 V vs. Zn^{2+}/Zn , appeared after approximately 200 cycles. These peaks were correlated with the developing plateau at around the same potential in the galvanostatic profiles. The first pair of peaks at around 1.6 V vs. Zn^{2+}/Zn , corresponded to the $\text{Fe}^{\text{III}}/\text{Fe}^{\text{II}}$ redox associated with the (de-)insertion of the Zn^{2+} , and the development of the second pair of peaks around 1.7 V vs. Zn^{2+}/Zn was correlated with the development of a two-phase insertion. In the case of the annealed electrodes, the second peaks at 1.7 V vs. Zn^{2+}/Zn were considerably sharper than that of the untreated electrode, particularly after approximately 300 cycles. We previously argued that the occurrence of such a two-phase insertion mechanism at higher potential compensates, at least partially, for the faded capacity of the material. This is the reason for the increased cycle life when the state of health is defined with respect to the specific energy (E) rather than the specific capacity (Q; refer to Table 1) [6,19].

There has been speculation that such phase transitions may affect the aging of CuHCF. In our previous work [6], we suggested that such phase transitions and changes in the potential profile may also be related to the formation of a different insertion site, with Zn^{2+} occupying vacancies in the CuHCF's host structure, followed by the nucleation of ZnHCF after long-term cycling.

All the annealed CuHCF electrodes showed very high coulombic efficiency ($\geq 99.5\%$), regardless of the temperature employed during the thermal treatment, as reported in Figure 11.

It is worth noting that the electrode with the longest cycle life, namely the 100 °C-annealed CuHCF, had an initial iron content of about 45% Fe^{III} and 55% Fe^{II} in its lattice (according to the ATR-FTIR analysis), while maintaining its structural stability (as demonstrated by the TGA). The better electrochemical performance (i.e., longer cycle life) of the material could have been due to the stabilizing effect on the crystal structure caused by the thermal treatment at 100 °C, which is likely to have provoked a rearrangement of the lattice. This lattice rearrangement might have been a consequence of a change in the amount/type of the defects present in the CuHCF's crystal structure, ultimately resulting in a change in the initial $\text{Fe}^{\text{III}}/\text{Fe}^{\text{II}}$ content ratio.

Since the tuning of CuHCF's properties through thermal treatment is limited by the possibility of the decomposition and structural deterioration of the lattice, other strategies should be developed in order to utilize an optimal $\text{Fe}^{\text{III}}/\text{Fe}^{\text{II}}$ content ratio in CuHCF crystal structures to achieve the best possible electrochemical performance.

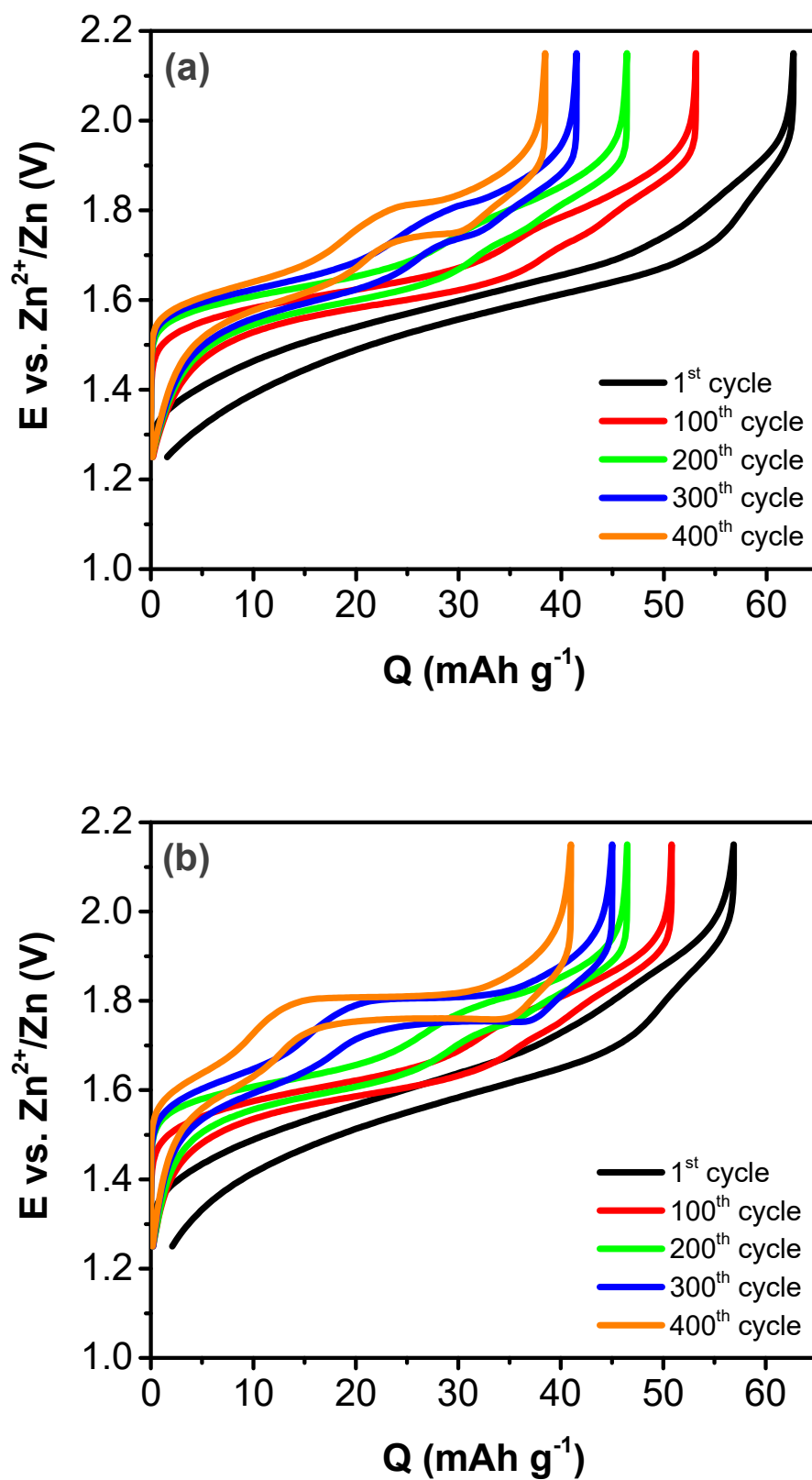


Figure 9. Galvanostatic cycles of (a) untreated and (b) 100 °C-annealed CuHCF electrodes, recorded at a C-rate of 1C.

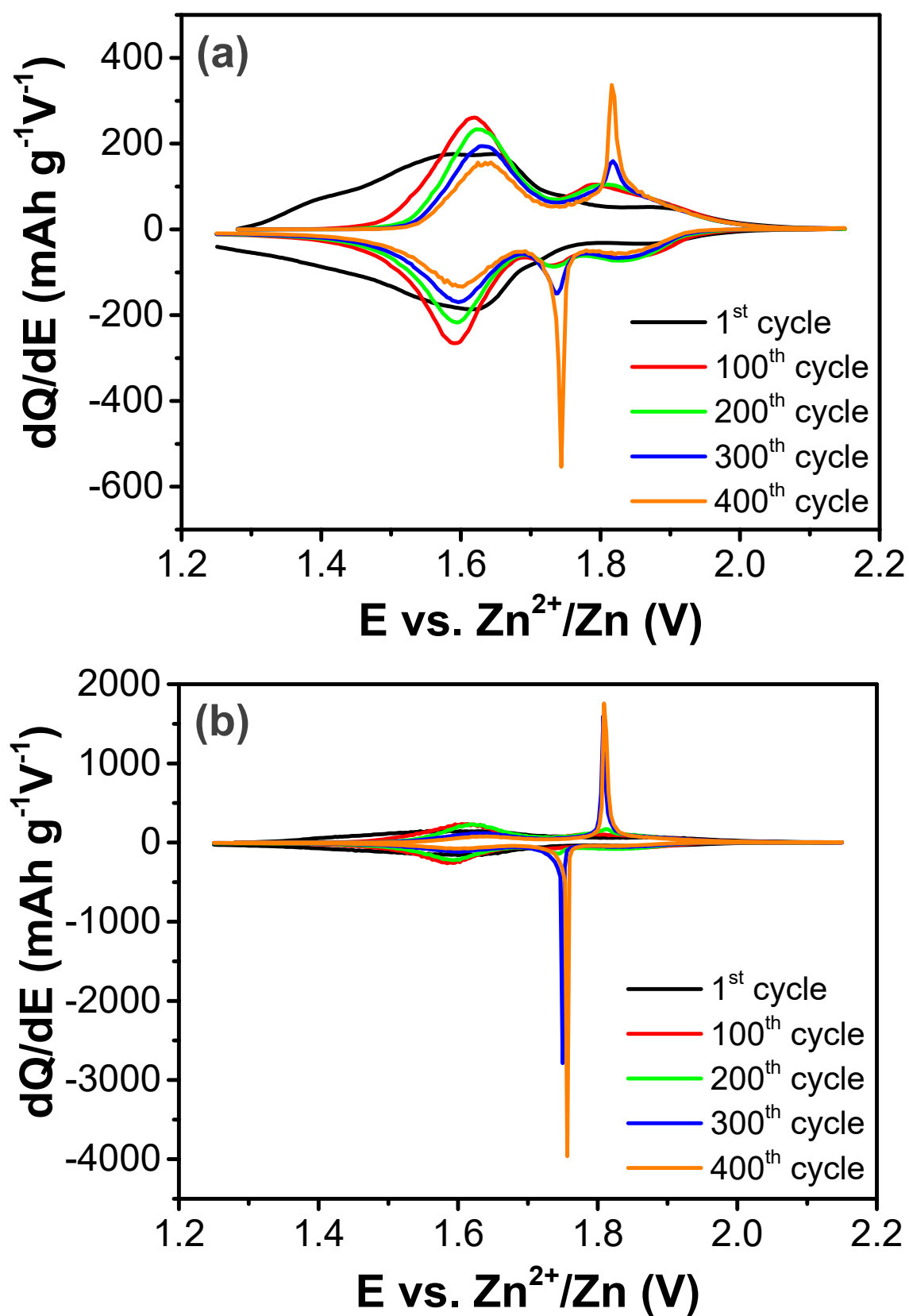


Figure 10. Differential charge plots for (a) untreated and (b) 100 °C-annealed CuHCF electrodes.

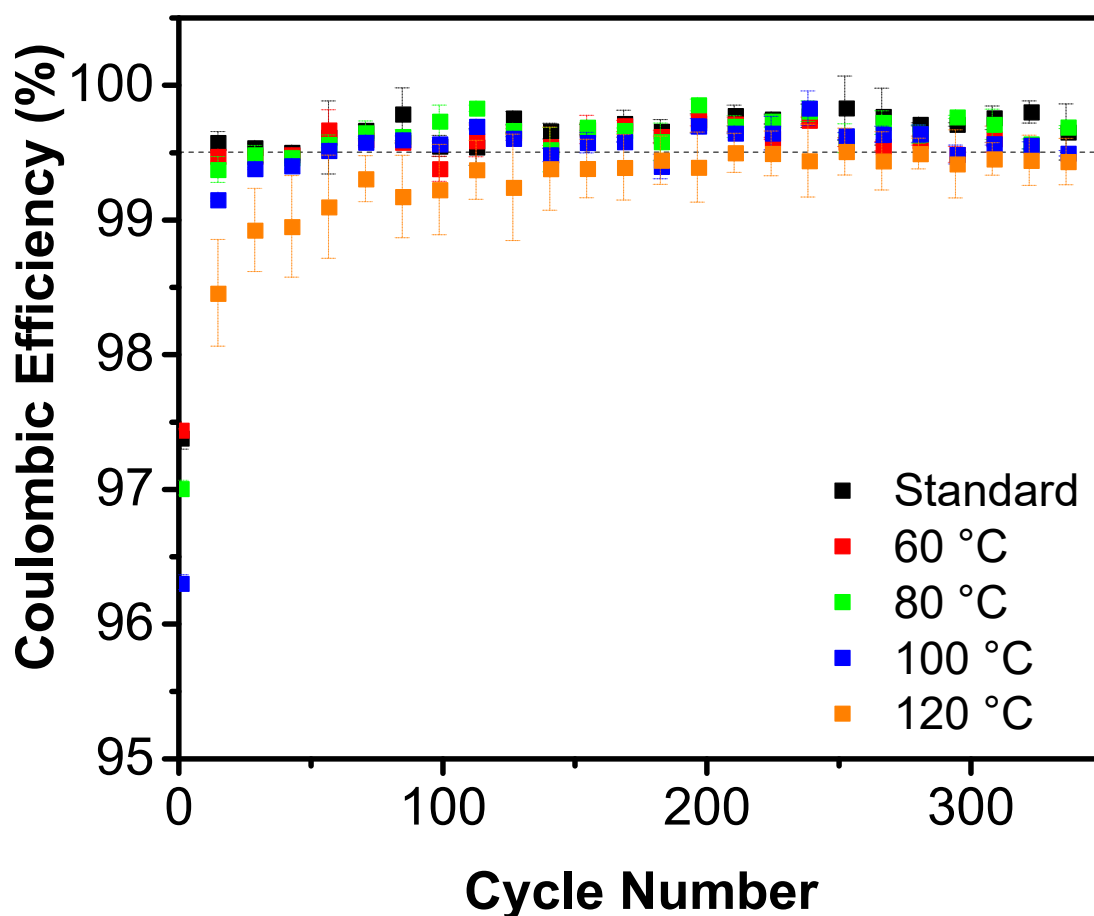


Figure 11. The mean value and standard deviation of coulombic efficiency of the synthesized CuHCF-based electrodes, annealed at different temperatures and galvanostatically cycled at 1C. The mean value and the standard deviations were calculated according to at least two different measurements of two different synthesis batches for each annealing temperature.

4. Conclusions

Here, structural changes in a CuHCF lattice were induced by thermally treating the material, with an apparent effect on its cycle life. In particular, it was found that our synthesized CuHCF is thermally stable up to nearly 120 °C. A structural analysis showed that the CuHCF's crystal lattice shrank upon increasing the annealing temperature. This change in crystal dimensions was attributed to a decrease in the lattice's $\text{Fe}^{\text{III}}/\text{Fe}^{\text{II}}$ content ratio, as suggested by our ATR-FTIR analyses, which was also in agreement with the values of the open-circuit potential of the annealed samples and with the initial oxidation charge during the first galvanostatic cycle of the samples. The galvanostatic cycling showed that the CuHCF-based electrode annealed at 100 °C, with a $\text{Fe}^{\text{III}}/(\text{Fe}^{\text{III}} + \text{Fe}^{\text{II}})$ content ratio in the range of 45%, exhibited a longer cycle life of ca. 400 cycles at 1C, compared to the 190 cycles reached by the untreated CuHCF.

Based on our experiments, it appears that the arrangement of elements in the crystal structure, particularly the $\text{Fe}^{\text{III}}/\text{Fe}^{\text{II}}$ content ratio in the crystal structure, may affect the stability of CuHCF lattices and, therefore, the electrochemical performance of CuHCF, when cycled in mild acidic aqueous electrolytes containing Zn^{2+} . Considering the challenges that are yet to be addressed to increase the stability of CuHCF when cycled in the presence of Zn ions, it is clear that thermal treatment is a suitable strategy to increase its cycle life and, therefore, accelerate the commercialization of aqueous Zn-ion batteries.

Supplementary Materials: The following supporting information can be downloaded at: <https://www.mdpi.com/article/10.3390/batteries9030170/s1>, Figure S1: SEM images of untreated and treated CuHCF powder; Figure S2: The first galvanostatic cycle of CuHCF-based electrodes; Figure S3: Galvanostatic cycles of all CuHCF-based electrodes; Figure S4: Differential charge plots of all CuHCF-based electrodes.

Author Contributions: Conceptualization, M.B., G.Z. and F.L.M.; formal analysis, M.B.; investigation, M.B. and J.G.; data curation, M.B. and G.Z.; writing—original draft preparation, M.B.; writing—review and editing, G.Z.; supervision, G.Z. and F.L.M.; project administration, F.L.M.; funding acquisition, F.L.M. All authors have read and agreed to the published version of the manuscript.

Funding: This research was funded by the German Federal Ministry of Education and Research (BMBF) grant number FKZ 03XP0204A.

Data Availability Statement: The data are available upon request from the corresponding authors.

Conflicts of Interest: The authors declare no conflict of interest.

References

- Delucchi, M.A.; Jacobson, M.Z. Providing All Global Energy with Wind, Water, and Solar Power, Part II: Reliability, System and Transmission Costs, and Policies. *Energy Policy* **2011**, *39*, 1170–1190. [CrossRef]
- Jacobson, M.Z.; Delucchi, M.A. Providing All Global Energy with Wind, Water, and Solar Power, Part I: Technologies, Energy Resources, Quantities and Areas of Infrastructure, and Materials. *Energy Policy* **2011**, *39*, 1154–1169. [CrossRef]
- Barton, J.P.; Infield, D.G. Energy Storage and Its Use with Intermittent Renewable Energy. *IEEE Trans. Energy Convers.* **2004**, *19*, 441–448. [CrossRef]
- Zampardi, G.; la Mantia, F. Prussian Blue Analogues as Aqueous Zn-Ion Batteries Electrodes: Current Challenges and Future Perspectives. *Curr. Opin. Electrochem.* **2020**, *21*, 84–92. [CrossRef]
- Zampardi, G.; la Mantia, F. Open Challenges and Good Experimental Practices in the Research Field of Aqueous Zn-Ion Batteries. *Nat. Commun.* **2022**, *13*, 687. [CrossRef] [PubMed]
- Zampardi, G.; Warnecke, M.; Tribbia, M.; Glenneberg, J.; Santos, C.; la Mantia, F. Effect of the Reactants Concentration on the Synthesis and Cycle Life of Copper Hexacyanoferrate for Aqueous Zn-Ion Batteries. *Electrochem. Commun.* **2021**, *126*, 107030. [CrossRef]
- Zhang, L.; Chen, L.; Zhou, X.; Liu, Z. Towards High-Voltage Aqueous Metal-Ion Batteries beyond 1.5 V: The Zinc/Zinc Hexacyanoferrate System. *Adv. Energy Mater.* **2015**, *5*, 1400930. [CrossRef]
- Yang, Z.; Zhang, J.; Kintner-Meyer, M.C.W.; Lu, X.; Choi, D.; Lemmon, J.P.; Liu, J. Electrochemical Energy Storage for Green Grid. *Chem. Rev.* **2011**, *111*, 3577–3613. [CrossRef]
- Blay, V.; Galian, R.E.; Muresan, L.M.; Pankratov, D.; Pinyou, P.; Zampardi, G.; Blay, V.; Galian, R.E.; Muresan, L.M.; Pankratov, D.; et al. Research Frontiers in Energy-Related Materials and Applications for 2020–2030. *Adv. Sustain. Syst.* **2020**, *4*, 1900145. [CrossRef]
- Kim, D.S.; Yoo, H.; Park, M.S.; Kim, H. Boosting the Sodium Storage Capability of Prussian Blue Nanocubes by Overlaying PEDOT:PSS Layer. *J. Alloys Compd.* **2019**, *791*, 385–390. [CrossRef]
- Xu, L.; Ma, J.; Guo, P.; Su, C. PEDOT-PSS-Coated FeFe(CN)₆ Composite Cathode for Lithium-Ion Batteries with the Improved Electrochemical Performances. *Nano* **2019**, *14*, 93–101. [CrossRef]
- Eckert, M.; Peters, W.; Drillet, J.F. Fast Microwave-Assisted Hydrothermal Synthesis of Pure Layered δ -MnO₂ for Multivalent Ion Intercalation. *Materials* **2018**, *11*, 2399. [CrossRef] [PubMed]
- Liu, Y.; Xie, L.; Zhang, W.; Dai, Z.; Wei, W.; Luo, S.; Chen, X.; Chen, W.; Rao, F.; Wang, L.; et al. Conjugated System of PEDOT:PSS-Induced Self-Doped PANI for Flexible Zinc-Ion Batteries with Enhanced Capacity and Cyclability. *ACS Appl. Mater. Interfaces* **2019**, *11*, 30943–30952. [CrossRef] [PubMed]
- Ming, J.; Guo, J.; Xia, C.; Wang, W.; Alshareef, H.N. Zinc-Ion Batteries: Materials, Mechanisms, and Applications. *Mater. Sci. Eng. R Rep.* **2019**, *135*, 58–84. [CrossRef]
- Li, Y.; Liu, B.; Ding, J.; Han, X.; Deng, Y.; Wu, T.; Amine, K.; Hu, W.; Zhong, C.; Lu, J. Understanding the Gap between Academic Research and Industrial Requirements in Rechargeable Zinc-Ion Batteries. *Batter. Supercaps* **2021**, *4*, 60–71. [CrossRef]
- Shin, J.; Lee, J.; Park, Y.; Choi, J.W. Aqueous Zinc Ion Batteries: Focus on Zinc Metal Anodes. *Chem. Sci.* **2020**, *11*, 2028–2044. [CrossRef]
- Oberholzer, P.; Tervoort, E.; Bouzid, A.; Pasquarello, A.; Kundu, D. Oxide versus Nonoxide Cathode Materials for Aqueous Zn Batteries: An Insight into the Charge Storage Mechanism and Consequences Thereof. *ACS Appl. Mater. Interfaces* **2019**, *11*, 674–682. [CrossRef] [PubMed]
- Tribbia, M.; Glenneberg, J.; Zampardi, G.; la Mantia, F. Highly Efficient, Dendrite-Free Zinc Electrodeposition in Mild Aqueous Zinc-Ion Batteries through Indium-Based Substrates. *Batter. Supercaps* **2022**, *5*, e202100381. [CrossRef]

19. Kasiri, G.; Glenneberg, J.; Kun, R.; Zampardi, G.; la Mantia, F. Microstructural Changes of Prussian Blue Derivatives during Cycling in Zinc-Containing Electrolytes. *ChemElectroChem* **2020**, *7*, 3301–3310. [\[CrossRef\]](#)
20. Gupta, T.; Kim, A.; Phadke, S.; Biswas, S.; Luong, T.; Hertzberg, B.J.; Chamoun, M.; Evans-Lutterodt, K.; Steingart, D.A. Improving the Cycle Life of a High-Rate, High-Potential Aqueous Dual-Ion Battery Using Hyper-Dendritic Zinc and Copper Hexacyanoferrate. *J. Power Sources* **2016**, *305*, 22–29. [\[CrossRef\]](#)
21. Jayalakshmi, M.; Scholz, F. Charge-Discharge Characteristics of a Solid-State Prussian Blue Secondary Cell. *J. Power Sources* **2000**, *87*, 212–217. [\[CrossRef\]](#)
22. Chen, R.; Huang, Y.; Xie, M.; Zhang, Q.; Zhang, X.; Li, L.; Wu, F. Preparation of Prussian Blue Submicron Particles with a Pore Structure by Two-Step Optimization for Na-Ion Battery Cathodes. *ACS Appl. Mater. Interfaces* **2016**, *8*, 16078–16086. [\[CrossRef\]](#) [\[PubMed\]](#)
23. Jayalakshmi, M.; Scholz, F. Performance Characteristics of Zinc Hexacyanoferrate/Prussian Blue and Copper Hexacyanoferrate/Prussian Blue Solid State Secondary Cells. *J. Power Sources* **2000**, *91*, 217–223. [\[CrossRef\]](#)
24. Widmann, A.; Kahlert, H.; Wulff, H.; Scholz, F. Electrochemical and Mechanochemical Formation of Solid Solutions of Potassium Copper(II)/Zinc(II) Hexacyanocobaltate(III)/Hexacyanoferrate(III) $\text{KCu}_x\text{Zn}_{1-x}[\text{Hcc}]_x[\text{Hcf}]_{1-x}$. *J. Solid State Electrochem.* **2005**, *9*, 380–389. [\[CrossRef\]](#)
25. Itaya, K.; Uchida, I.; Neff, V.D. *Mixed-Valence Compounds; Theory and Applications in Chemistry*; Nato Advanced Study Institutes Series D; Reidel: Dordrecht, The Netherlands, 1986; Volume 19, p. 4575.
26. Soto, M.B.; Scholz, F. The Thermodynamics of the Insertion Electrochemistry of Solid Metal Hexacyanometallates. *J. Electroanal. Chem.* **2002**, *521*, 183–189. [\[CrossRef\]](#)
27. Doménech, A.; Montoya, N.; Scholz, F. Estimation of Individual Gibbs Energies of Cation Transfer Employing the Insertion Electrochemistry of Solid Prussian Blue. *J. Electroanal. Chem.* **2011**, *657*, 117–122. [\[CrossRef\]](#)
28. Wang, X.; Wang, B.; Tang, Y.; Bin Xu, B.; Liang, C.; Yan, M.; Jiang, Y. Manganese Hexacyanoferrate Reinforced by PEDOT Coating towards High-Rate and Long-Life Sodium-Ion Battery Cathode. *J. Mater. Chem. A* **2020**, *8*, 3222–3227. [\[CrossRef\]](#)
29. Shkreba, E.V.; Apraksin, R.V.; Tolstopjatova, E.G.; Kondratiev, V.V. Cathode Material for Sodium-Ion Batteries Based on Manganese Hexacyanoferrate: The Role of the Binder Component. *J. Solid State Electrochem.* **2020**, *24*, 3049–3057. [\[CrossRef\]](#)
30. Liu, S.; Pan, G.L.; Li, G.R.; Gao, X.P. Copper Hexacyanoferrate Nanoparticles as Cathode Material for Aqueous Al-Ion Batteries. *J. Mater. Chem. A* **2014**, *3*, 959–962. [\[CrossRef\]](#)
31. Jia, Z.; Wang, B.; Wang, Y. Copper Hexacyanoferrate with a Well-Defined Open Framework as a Positive Electrode for Aqueous Zinc Ion Batteries. *Mater. Chem. Phys.* **2015**, *149–150*, 601–606. [\[CrossRef\]](#)
32. Xue, Q.; Li, L.; Huang, Y.; Huang, R.; Wu, F.; Chen, R. Polypyrrole-Modified Prussian Blue Cathode Material for Potassium Ion Batteries via in Situ Polymerization Coating. *ACS Appl. Mater. Interfaces* **2019**, *11*, 22339–22345. [\[CrossRef\]](#)
33. Hong, S.F.; Chen, L.C. Nano-Prussian Blue Analogue/PEDOT:PSS Composites for Electrochromic Windows. *Sol. Energy Mater. Sol. Cells* **2012**, *104*, 64–74. [\[CrossRef\]](#)
34. Kjeldgaard, S.; Wagemaker, M.; Iversen, B.B.; Bentien, A. Sample Dependent Performance of Aqueous Copper Hexacyanoferrate/Zinc Batteries. *Mater. Adv.* **2021**, *2*, 2036–2044. [\[CrossRef\]](#)
35. Renman, V.; Ojwang, D.O.; Valvo, M.; Gómez, C.P.; Gustafsson, T.; Svensson, G. Structural-Electrochemical Relations in the Aqueous Copper Hexacyanoferrate-Zinc System Examined by Synchrotron X-Ray Diffraction. *J. Power Sources* **2017**, *369*, 146–153. [\[CrossRef\]](#)
36. Zampardi, G.; Sokolov, S.V.; Batchelor-McAuley, C.; Compton, R.G. Potassium (De-)Insertion Processes in Prussian Blue Particles: Ensemble versus Single Nanoparticle Behaviour. *Chem. A Eur. J.* **2017**, *23*, 14338–14344. [\[CrossRef\]](#) [\[PubMed\]](#)
37. Zampardi, G.; Compton, R.G. Fast Electrodeposition of Zinc onto Single Zinc Nanoparticles. *J. Solid State Electrochem.* **2020**, *24*, 2695–2702. [\[CrossRef\]](#)
38. Ojwang, D.O.; Grins, J.; Wardecki, D.; Valvo, M.; Renman, V.; Häggström, L.; Ericsson, T.; Gustafsson, T.; Mahmoud, A.; Hermann, R.P.; et al. Structure Characterization and Properties of K-Containing Copper Hexacyanoferrate. *Inorg. Chem.* **2016**, *55*, 5924–5934. [\[CrossRef\]](#)
39. Kuperman, N.; Cairns, A.; Goncher, G.; Solanki, R. Structural Water Enhanced Intercalation of Magnesium Ions in Copper Hexacyanoferrate Nonaqueous Batteries. *Electrochim. Acta* **2020**, *362*, 137077. [\[CrossRef\]](#)
40. Görlin, M.; Ojwang, D.O.; Lee, M.T.; Renman, V.; Tai, C.W.; Valvo, M. Aging and Charge Compensation Effects of the Rechargeable Aqueous Zinc/Copper Hexacyanoferrate Battery Elucidated Using in Situ X-Ray Techniques. *ACS Appl. Mater. Interfaces* **2021**, *13*, 59962–59974. [\[CrossRef\]](#)
41. Gerber, S.J.; Erasmus, E. Electronic Effects of Metal Hexacyanoferrates: An XPS and FTIR Study. *Mater. Chem. Phys.* **2018**, *203*, 73–81. [\[CrossRef\]](#)
42. Ng, C.W.; Ding, J.; Shi, Y.; Gan, L.M. Structure and Magnetic Properties of Copper(II) Hexacyanoferrate(III) Compound. *J. Phys. Chem. Solids* **2001**, *62*, 767–775. [\[CrossRef\]](#)
43. Trócoli, R.; la Mantia, F. An Aqueous Zinc-Ion Battery Based on Copper Hexacyanoferrate. *ChemSusChem* **2015**, *8*, 481–485. [\[CrossRef\]](#) [\[PubMed\]](#)
44. Moloney, M.P.; Massoni, N.; Grandjean, A. Tuning the Thermal Stability of Copper(II) Hexacyanoferrate(II) Nanoparticles. *J. Therm. Anal. Calorim.* **2020**, *145*, 2353–2362. [\[CrossRef\]](#)

45. Shi, N.; Gao, Q.; Sanson, A.; Li, Q.; Fan, L.; Ren, Y.; Olivi, L.; Chen, J.; Xing, X. Negative Thermal Expansion in Cubic $\text{FeFe}(\text{CN})_6$ Prussian Blue Analogues. *Dalton Trans.* **2019**, *48*, 3658–3663. [[CrossRef](#)]
46. Hu, J.; Tao, H.; Chen, M.; Zhang, Z.; Cao, S.; Shen, Y.; Jiang, K.; Zhou, M. Interstitial Water Improves Structural Stability of Iron Hexacyanoferrate for High-Performance Sodium-Ion Batteries. *ACS Appl. Mater. Interfaces* **2022**, *14*, 12234–12242. [[CrossRef](#)]
47. Hesse, H.C.; Schimpe, M.; Kucevic, D.; Jossen, A. Lithium-Ion Battery Storage for the Grid—A Review of Stationary Battery Storage System Design Tailored for Applications in Modern Power Grids. *Energies* **2017**, *10*, 2107. [[CrossRef](#)]

Disclaimer/Publisher’s Note: The statements, opinions and data contained in all publications are solely those of the individual author(s) and contributor(s) and not of MDPI and/or the editor(s). MDPI and/or the editor(s) disclaim responsibility for any injury to people or property resulting from any ideas, methods, instructions or products referred to in the content.